Available online at www.sciencedirect.com
SCIENCE DIRECT®
PERGAMON
International Journal of Multiphase Flow 29 (2003) 1413–1430
International Journal of Multiphase Flow
www.elsevier.com/locate/ijmulflow

Analysis of liquid film formation in a horizontal annular flow by DNS

T. Fukano [a,*], T. Inatomi [b]

[a] *Department of Mechanical Engineering Science, Faculty of Engineering, Kyushu University, 6-10-1, Hakozaki, Higashi-ku, Fukuoka 812-8581, Japan*
[b] *Reactor Component Design Group, Nuclear Energy Equipment Manufacturing Department, Keihin Product Operations, Power Systems and Services Company, Toshiba Corporation, 2-4, Suehiro-cho, Tsurumi-ku, Yokohama 230-0045, Japan*

Received 15 April 2002; received in revised form 11 June 2003

Abstract

The role of the disturbance waves for transferring liquid toward the top of a horizontal tube wall to cope with the drainage due to gravity is investigated by the direct numerical simulation (DNS) which is based on the continuity equation and the Navier–Stokes equations in three-dimensional cylindrical coordinate system. The level set method is used for capturing the interface between gas–liquid two fluids. Developing flow from a separated to an annular flow is simulated by using this numerical technique, and the liquid film formation is reproduced. It is demonstrated by this calculation result that liquid is transferred in the circumferential direction as the liquid film by the pumping action of disturbance waves which has been proposed by one of the present authors. That is, the pressure gradient formed within a disturbance wave in the circumferential direction plays an important role for the liquid film formation in a horizontal annular flow.

Keywords: Two-phase flow; Gas–liquid annular flow; Numerical analysis; Horizontal tube; Disturbance wave; Pumping action

1. Introduction

Gas–liquid two-phase annular flow in a horizontal tube occurs in a wide variety of industrial processes. When the liquid fraction is small in horizontal annular flow, it is possible to cause an

* Corresponding author. Tel./fax: +81-92-642-3392.
E-mail address: fukanot@mech.kyushu-u.ac.jp (T. Fukano).

0301-9322/$ - see front matter
doi:10.1016/S0301-9322(03)00127-7

extremely important problem that relates to the damage of heat exchanger tubes, because the drainage of liquid due to gravity, as well as the evaporation, leads to the dryout of thin liquid film near the top of the tube. Therefore, it is important to accurately predict the circumferential distribution of film thickness in horizontal annular flow. For this end, it is necessary that the mechanism of the liquid film formation up to the upper part of the tube is fully investigated and modeled.

In theoretical researches into the circumferential distribution of the liquid film thickness in gas–liquid horizontal two-phase annular flow, the discussion has been focused on the mechanism for transferring liquid towards the top of the tube. They are the following four mechanisms.

(1) Secondary gas flow mechanism (Laurinat et al., 1985; Lin et al., 1985; Flores et al., 1995).
(2) Liquid entrainment and deposition mechanism (Russell and Lamb, 1965).
(3) Wave spreading and mixing mechanism (Butterworth and Pulling, 1972; Jayanti et al., 1990).
(4) Pumping action of a disturbance wave (Fukano and Ousaka, 1989; Sutharshan et al., 1995).

A detailed mechanism that liquid is transferred in the circumferential direction has not been clarified so far, though it is understood that the disturbance waves play the most important role. It is difficult experimentally to investigate in detail the mechanism of the liquid film formation because the annular flow is highly unsteady in the disturbance wave region. In the present paper, the role of the disturbance waves is investigated by the DNS and the models of the liquid film formation proposed so far are evaluated.

2. Equations of motion

In the present paper a direct numerical simulation of the generation of disturbance wave and the liquid film formation in a horizontal tube has been done based on a level set method (Osher and Sethian, 1988; Sussman et al., 1994; Chang et al., 1996) which is used for representing and capturing the interface between gas–liquid two fluids. The incompressible Navier–Stokes equations, continuity equation, and advection equation of the level set function ϕ in three-dimensional cylindrical coordinate system are used as the governing equations. Those equations can be discretized without any singularity such as points on the axis of a tube by means of the formulation proposed by Verzicco and Orlandi (1996) and be written as follows with the quantities $q_r = ru_r$, $q_\theta = u_\theta$, and $q_z = u_z$ where u_r, u_θ, and u_z are the velocity components in the r, θ, and z directions, respectively.

The continuity equation is expressed as follow:

$$\frac{1}{r}\frac{\partial q_r}{\partial r} + \frac{1}{r}\frac{\partial q_\theta}{\partial \theta} + \frac{\partial q_z}{\partial z} = 0 \tag{1}$$

In terms of q_r, q_θ, and q_z, the momentum equations in non-conservative form become

$$\begin{aligned}\frac{\partial q_r}{\partial t} + q_r\frac{\partial}{\partial r}\left(\frac{q_r}{r}\right) + \frac{q_\theta}{r}\frac{\partial q_r}{\partial \theta} + q_z\frac{\partial q_r}{\partial z} - q_\theta^2 \\ = -\frac{r}{\rho(\phi)}\frac{\partial p}{\partial r} + \frac{1}{\rho(\phi)}\left[2\frac{\partial}{\partial r}\left(\mu(\phi)\frac{\partial q_r}{\partial r}\right) + \frac{\partial}{\partial \theta}\left(\mu(\phi)r\frac{\partial}{\partial r}\left(\frac{q_\theta}{r}\right) + \frac{\mu(\phi)}{r^2}\frac{\partial q_r}{\partial \theta}\right)\right.\end{aligned}$$

$$+\frac{\partial}{\partial z}\left(\mu(\phi)\frac{\partial q_r}{\partial z}+\mu(\phi)\frac{\partial q_z}{\partial r}\right)-\frac{2}{r}\frac{\partial}{\partial r}(\mu(\phi)q_r)-2\frac{\mu(\phi)}{r}\frac{\partial q_\theta}{\partial \theta}\Bigg]$$
$$-r\frac{1}{\rho(\phi)}\sigma\kappa(\phi)\delta(\phi)\frac{\partial\phi}{\partial r}-rg\sin\theta \tag{2}$$

$$\frac{\partial q_\theta}{\partial t}+\frac{q_r}{r}\frac{\partial q_\theta}{\partial r}+\frac{q_\theta}{r}\frac{\partial q_\theta}{\partial \theta}+q_z\frac{\partial q_\theta}{\partial z}+\frac{q_r q_\theta}{r^2}$$
$$=-\frac{1}{\rho(\phi)r}\frac{\partial p}{\partial\theta}+\frac{1}{\rho(\phi)}\left[\frac{1}{r^2}\frac{\partial}{\partial r}\left(\mu(\phi)r^3\frac{\partial}{\partial r}\left(\frac{q_\theta}{r}\right)+\mu(\phi)\frac{\partial q_r}{\partial\theta}\right)+\frac{2}{r}\frac{\partial}{\partial\theta}\left(\frac{\mu(\phi)}{r}\frac{\partial q_\theta}{\partial r}+\mu(\phi)\frac{q_r}{r^2}\right)\right.$$
$$\left.+\frac{\partial}{\partial z}\left(\frac{\mu(\phi)}{r}\frac{\partial q_z}{\partial\theta}+\mu(\phi)\frac{\partial q_\theta}{\partial z}\right)\right]-\frac{1}{\rho(\phi)}\sigma\kappa(\phi)\delta(\phi)\frac{1}{r}\frac{\partial\phi}{\partial\theta}-g\cos\theta \tag{3}$$

$$\frac{\partial q_z}{\partial t}+\frac{q_r}{r}\frac{\partial q_z}{\partial r}+\frac{q_\theta}{r}\frac{\partial q_z}{\partial\theta}+q_z\frac{\partial q_z}{\partial z}=-\frac{1}{\rho(\phi)}\frac{\partial p}{\partial z}+\frac{1}{\rho(\phi)}\left[\frac{1}{r}\frac{\partial}{\partial r}\left(\mu(\phi)\frac{\partial q_r}{\partial z}+\mu(\phi)r\frac{\partial q_z}{\partial r}\right)\right.$$
$$\left.+\frac{1}{r}\frac{\partial}{\partial\theta}\left(\frac{\mu(\phi)}{r}\frac{\partial q_z}{\partial\theta}+\mu(\phi)\frac{\partial q_\theta}{\partial z}\right)+2\frac{\partial}{\partial z}\left(\mu(\phi)\frac{\partial q_z}{\partial z}\right)\right]$$
$$-\frac{1}{\rho(\phi)}\sigma\kappa(\phi)\delta(\phi)\frac{\partial\phi}{\partial z} \tag{4}$$

where ρ is the density and μ the viscosity, g the gravitational acceleration, p the pressure, κ and δ the curvature and delta function, respectively, and σ the surface tension. In the present paper, the model of continuum surface force (CSF) is employed to treat the surface tension on the interface. The advection equation of the level set function ϕ is given by

$$\frac{\partial\phi}{\partial t}+\frac{q_r}{r}\frac{\partial\phi}{\partial r}+\frac{q_\theta}{r}\frac{\partial\phi}{\partial\theta}+q_z\frac{\partial\phi}{\partial z}=0 \tag{5}$$

3. Numerical formulation

3.1. Level set method

To calculate two-phase flow with free surfaces is generally difficult. The level set method proposed by Osher and Sethian (1988) to solve this problem is recently being generalized by Sussman et al. (1994) and Chang et al. (1996). The level set function ϕ is usually defined as the signed distance from the interface in the entire computational domain and $\phi = 0$ at the interface.

$$\Gamma=\{\mathbf{x}|\phi(\mathbf{x},t)=0\} \tag{6}$$

We take $\phi<0$ in the gas phase and $\phi>0$ in the liquid phase. Therefore, we have

$$\phi(\mathbf{x},t)\begin{cases}<0 & \text{if } \mathbf{x}\in\text{Gas}\\ =0 & \text{if } \mathbf{x}\in\Gamma\\ >0 & \text{if } \mathbf{x}\in\text{Liquid}\end{cases} \tag{7}$$

The unit normal on the interface **n**, drawn from the gas phase into the liquid phase, and the curvature of the interface $\kappa(\phi)$ are expressed in terms of $\phi(\mathbf{x}, t)$, respectively as:

$$\mathbf{n} = \left.\frac{\nabla\phi}{|\nabla\phi|}\right|_{\phi=0} \quad \text{and} \quad \kappa(\phi) = \nabla \cdot \frac{\nabla\phi}{|\nabla\phi|} \tag{8}$$

The density ρ and the viscosity μ are defined by the following equations, respectively.

$$\rho(\phi) = \rho_G + (\rho_L - \rho_G)H(\phi) \tag{9}$$

and

$$\mu(\phi) = \mu_G + (\mu_L - \mu_G)H(\phi) \tag{10}$$

where the suffixes L and G stand for liquid and gas phase, respectively. $H(\phi)$ is the Heaviside function defined by

$$H(\phi) = \begin{cases} 0 & \text{if } \phi < -\alpha \\ 1/2[1 + \phi/\alpha + 1/\pi \sin(\pi\phi/\alpha)] & \text{if } |\phi| \leqslant \alpha \\ 1 & \text{if } \phi > \alpha \end{cases} \tag{11}$$

The smoothed delta function is defined as,

$$\delta(\phi) = \begin{cases} 1/2[1 + \cos(\pi\phi/\alpha)]/\alpha & |\phi| < \alpha \\ 0 & \text{otherwise} \end{cases} \tag{12}$$

$$\alpha = 3/2\sqrt{(\Delta r)_{\min} \times (r\Delta\theta)_{\max}} \tag{13}$$

where α is the prescribed thickness of the interface. $(\Delta r)_{\min}$ and $(r\Delta\theta)_{\max}$ are grid spacings near the wall, respectively and are shown in Table 1. Therefore, $\alpha = 0.702$ mm in the present calculation.

3.2. Re-initialization of level set function and mass conservation

Initially, the level set function ϕ is set as a signed distance from the interface. It, however, does not remain a distance function anymore after long calculation, and re-initialization is a necessary and critical step. The re-initialization procedure proposed by Sussman et al. (1994) is used here for keeping ϕ as an object function at all times. This is accomplished by repeatedly solving the following equation to reach a steady state:

$$\frac{\partial\phi}{\partial\tau} = S(\phi_0)(1 - |\nabla\phi|) \tag{14}$$

where S is the sign function. For numerical stability, it is useful to smooth the sign function as follow:

Table 1
Grid numbers and grid resolution

Grid numbers $r \times \theta \times z$	L (mm)	D (mm)	$\Delta r_{\max}$ (mm)	$\Delta r_{\min}$ (mm)	$(r\Delta\theta)_{\max}$ (mm)	$(r\Delta\theta)_{\min}$ (mm)	Δz (mm)
32×64×200	1000	26	0.784	0.173	1.27	0.039	5.0

$$S(\phi_0) = \phi_0 \Big/ \sqrt{\phi_0^2 + \alpha^2} \tag{15}$$

where ϕ_0 is the previous level set function before the re-initialization. The solution of ϕ has the same sign and the same level set as ϕ_0 and satisfies $|\nabla\phi| = 1$. It is therefore a distance function from the interface. Here, τ is independent of t in the main routine, and it is taken as constant, $\tau = 2 \times 10^{-5}$ s in the present calculation. Even with the above re-initialization procedure, the loss of mass occurs. In fact, the numerical discretization of the level set formulation does not guarantee the mass conservation. To overcome this difficulty, a second re-initialization procedure is devised, which is similar to that proposed by Chang et al. (1996) with a goal of preserving the global mass at each time step. This requires to solve the following equation to a steady state:

$$\frac{\partial\phi}{\partial\tau} + \left[1 - \frac{A(\tau)}{A_0(t)}\right] F(\mathrm{vc})|\nabla\phi| = 0 \tag{16}$$

where $A_0(t)$ is the total mass in a whole calculation domain, $A(\tau)$ the total mass corresponding to the level set function $\phi(\tau)$, and $F(\mathrm{vc})$ the volume constraint function. Here, the time step $\Delta\tau = 2 \times 10^{-3}$ s was used.

For the free surface, $F(\mathrm{vc})$ can be considered as a function of the local curvature and defined as follow:

$$F(\mathrm{vc}) = -1.0 + \beta\kappa^n \tag{17}$$

where β and n are constant. The $F(\mathrm{vc})$ is related to the local mass conservation, which vary with β and n. The re-initialization procedure converges much faster when $\beta = 0$ and $n = 0$, which are used in the present calculation. By this way the total mass is conserved within 0.01%.

3.3. Numerical procedure

We solved numerically the equations derived in the previous sections by using a finite difference method. A staggered mesh was used for the velocity and the level set function. The advection terms were discretized by the K.K. scheme (Kawamura and Kuwahara, 1984) as the third-order upwind difference method and the other terms by the central finite difference method. The K.K. scheme has been reported to be useful for the calculation of a turbulent flow and we did not use any particular turbulence model in the calculation. And the SMAC method (Amsden and Harlow, 1970) was used as an algorithm for the time quadrature. The Euler method was used as the time integration scheme. The Poisson's equation was solved by an incomplete LU decomposition bi-conjugate gradient stabilized (ILU-Bi-CGSTAB) method. The time step Δt was determined by the restrictions due to the CFL condition, gravity, viscosity, and surface tension. In this calculation, the CFL restriction of 0.1 or 0.2 was used.

The outline of our scheme is as follow. For given ϕ^n, u^n, and p^n defined at each cell, we solved for ϕ^{n+1}, u^{n+1} and p^{n+1}. For each time step:

Step 1: $\phi(\mathbf{x}, t)$ is initialized, and an initial distribution of liquid film thickness is determined.
Step 2: The functions of $\rho(\phi)$, $\mu(\phi)$, and the surface tension are respectively determined. The K.K. scheme is used as the upwind difference method for the advective terms and

the central difference method is used for other differences. Then, the governing equations for $\boldsymbol{q}^n$ are discretized, and the intermediate quantity $\boldsymbol{q}^*$ is obtained.

Step 3: The Poisson's equation of pressure is solved by using an ILU-Bi-CGSTAB method, the quantity and pressure are updated, and $\boldsymbol{q}^{n+1}$ and p^{n+1} are obtained, respectively.

Step 4: The level set function ϕ^n is solved by using the K.K. scheme and $\phi^{n+1/2}$ is obtained.

Step 5: Because $\phi^{n+1/2}$ is not a signed distance function from the interface any longer, it is re-initialized and is updated to ϕ^{n+1}.

Step 6: Repeat steps 2–5.

3.4. Boundary conditions

The computational domain and boundary conditions are shown in Fig. 1. The inner diameter and the length of the tube are 26 mm and 1.0 m, respectively. The grid numbers, as shown in Table 1, are 32, 64, and 200 in the r, θ, and z directions, respectively. The grid spacing in the radial direction is small near the wall, and gradually widens toward the tube center. Meanwhile the grid spacing is equal circumferentially and axially.

At the inlet boundary, the inflow axial velocity and the film thickness are kept constant. At the outlet boundary, the velocity and the level set function are determined by use of the convective boundary condition, that is, the upwind finite difference of the advection equation. The non-slip condition is used at the wall. Wetting of the wall surface is represented by transferring the level set function with the consideration of the contact angle only near the edge of the liquid film contacting the wall. Here, the contact angle is assumed to be constant, $\theta = 30°$, in the calculation.

It is necessary to give an initial small disturbance so that the wave may quickly grow in the initial stage of its development. The incipient wave pattern is given by the sine function as the initial disturbance by one wavelength from the inlet. The amplitude of the wave is 3% of the maximum film thickness, and the wavelength is determined by referring to the average size of the disturbance wave obtained experimentally in a horizontal gas–liquid two-phase annular flow by Fukano et al. (1983).

3.5. Initial conditions

The initial conditions of the axial velocity, film thickness distribution, and pressure gradient $\partial p/\partial z$ are obtained by solving the following equation.

$$\frac{\partial p}{\partial z} = \frac{1}{r}\frac{\partial}{\partial r}\left(\mu(\phi) r \frac{\partial u_z}{\partial r}\right) + \frac{1}{r^2}\frac{\partial}{\partial \theta}\left(\mu(\phi)\frac{\partial u_z}{\partial \theta}\right) \tag{18}$$

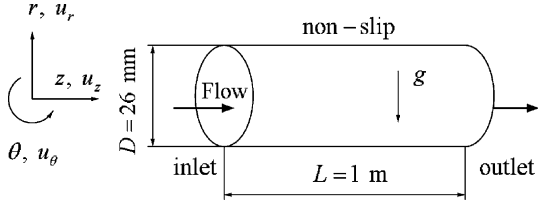

Fig. 1. Computational domain and boundary conditions.

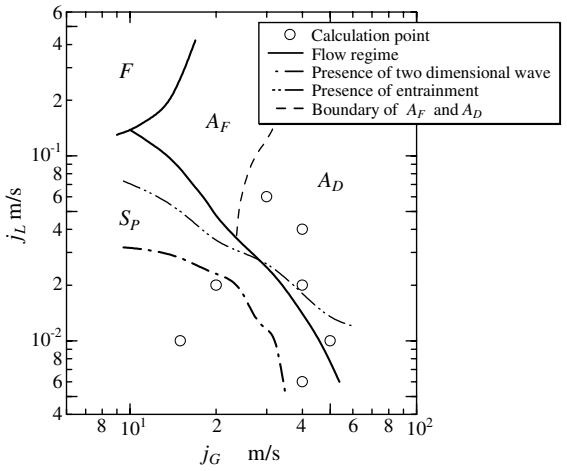

Fig. 2. Calculation points on a flow regime map.

The local value of u_z is determined by Eq. (18) with the successive bisection method if $\partial p/\partial z$ and the inlet liquid film distribution are given. The calculation is repeated until the superficial velocities of the both gas and liquid phases, j_G and j_L determined by u_z satisfy the required condition. Then, the velocity distribution with a constant fraction of gas and liquid and the film thickness distribution are uniformly given in the entire domain as an initial condition.

3.6. Numerical conditions

The flow patterns experimentally observed by Fukano et al. (1983) are classified into annular, froth, and separated flows, which are respectively indicated as A, F, S_P in Fig. 2. The mark O indicates the present calculation point. We calculate mainly near the boundary between A_D and S_P, where A_D means the disturbance annular flow. The property of air and water at 20 °C was used. The ranges of Reynolds number of gas and liquid are $Re_G = 25\,743$–$85\,806$ and $Re_L = 155$–554, respectively. In the present paper, we will discuss the results only in the case of the superficial velocity of gas and liquid: $j_G = 30$ m/s and $j_L = 0.06$ m/s, respectively.

4. Results and discussion

4.1. Formation process of annular flow

Fig. 3 shows the time evolution of the waves and annular flow formation. The direction of flow is shown by an arrow. A minute disturbance, which is given as an initial condition in the limited region close to the inlet, develops gradually to be waves in the range of $z < 400$ mm at $t = 0.164$ s. At $t = 0.168$ s one of the waves is about to grow up rapidly in the height direction of the tube and the wave also rapidly spreads in the circumferential direction at $t = 0.172$ s. And then it reaches the top of the tube at $t = 0.176$ s. On the other hand, the new waves, which are generated in the

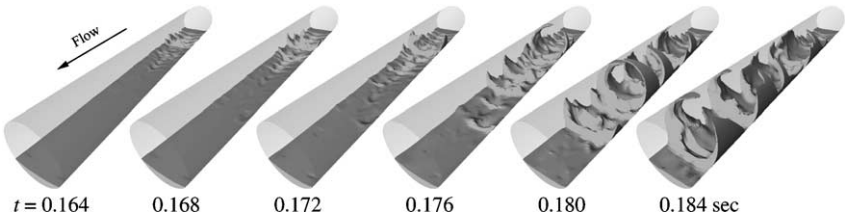

Fig. 3. Process of annular flow formation in A_D regime: $j_G = 30$ m/s, $j_L = 0.06$ m/s.

downstream region of the large wave by vortices discharged from the large wave, grow up rapidly to be an almost annular ring at $t = 0.180$ s. About five large waves form in the whole calculation region, and each wave seems to line up in a certain interval though it is different in size. The overall structure can be called as an annular flow.

Although in the present study the length L of the calculation region is very short, and the grid spacing Δz of 5.0 mm is rough, it was shown that an annular flow was reproduced by the present calculation technique as shown in Fig. 3 under the flow conditions in the annular flow regime as shown in Fig. 2.

Fig. 4 shows the pressure loss between the inlet and the outlet of the tube. At the beginning of the calculation, it is very low because the interface is smooth without waves, and then begins to increase rapidly at $t = 0.150$ s after increasing gradually as the waves continues to glow on the interface. This rapid increase in the pressure loss is caused by the increase of the friction loss on the liquid film surface. The broken line in the figure indicates the experimental result by Ousaka et al. (1985). The calculation result is still smaller than the experimental result at the end of the calculation because the computation time is short for the flow to be fully developed and the smooth surface exists always near the inlet as the inlet condition. Actually, this calculation was stopped at $t = 0.188$ s when the large wave reached at the exit.

Close inspection of the time evolution of the static pressure distribution on the interface reveals the formation process of an annular flow more in detail. Fig. 5 shows the flow development in the case of the same flow condition as Fig. 3, but the flow direction is opposite so that the pressure distribution generated on the surface behind the wave can be observed. The shape of the liquid

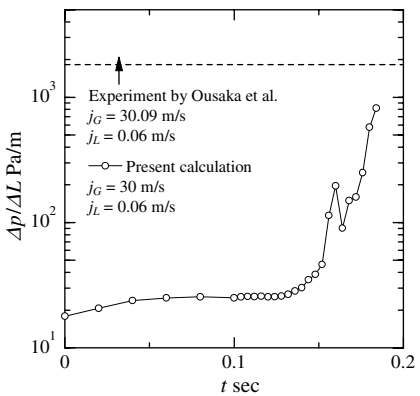

Fig. 4. Pressure loss in the process of annular flow formation.

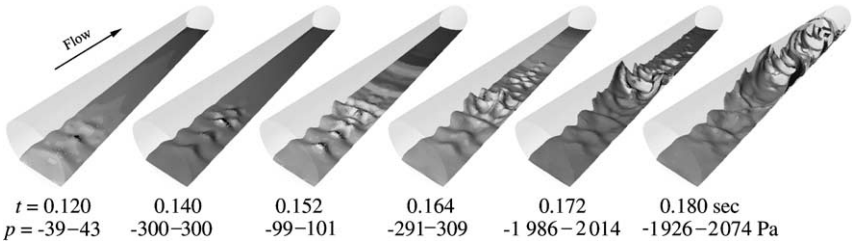

Fig. 5. Change in the pressure distribution on the interface.

film is also shown at the same time, while Fig. 5 indicates the pressure distribution at the interface. The contour of the pressure is displayed on the wavy surface by 12 color levels, i.e., the stronger the white level, the higher the pressure, and the stronger the black, the lower. The ranges of the maximum and minimum pressure are shown at the bottom of each figure by the unit of Pa. The reference pressure is 0.0 Pa at the top of the outlet cross-section.

At $t = 0.120$ s the pressure is already high behind the waves though the waves do not grow large yet. On the other hand, the wave crest is darker because the gas flow is fast, i.e., the pressure is low there. At $t = 0.140$ s, the waves grow up a little, the pressure has increased especially behind the relatively large wave, and descended from the top of the wave to the front. A large pressure difference between the front and the rear of the wave has been caused even in such a small wave. On the other hand, the pressure gradient is generated in the circumferential direction from the back of the wave toward the side wall. At $t = 0.152$ s the liquid film has spread in the circumferential direction of the tube by the pressure gradient. At $t = 0.164$ s the wave is about to grow up in the height direction, and the pressure has risen sideward along the wave. At $t = 0.172$ s the pressure gradient develops from the bottom of the tube in the circumferential direction. Therefore, the liquid film is transferred from the bottom to the side wall, about $\theta = 120°$. At $t = 0.180$ s the waves in the downstream region also develop rapidly, and the liquid film is transferred up to near the top of the tube. The pressure is the highest at the bottom with thick film thickness and gradually decreases as the film thickness decreases toward the top. As described above, this calculation result indicates the same tendency as "the pumping action of a disturbance wave" which Fukano and Ousaka (1989) have proposed.

Fig. 6 shows the distribution of the film thickness or the height of the interface by 12 levels of brightness. The darker the color is, the thinner the film. When the liquid film does not exist on the wall, white is used for convenience. It must be noticed, however, that very thin liquid film less than one radial mesh size might exist in an actual annular flow. The vertical axis implies the circumferential position with $\theta = 0°$ at the bottom of the tube and $\theta = 180°$ and $-180°$ at the top of the tube. The horizontal axis is the axial distance. The arrow shows the direction of flow. "A" in the figure indicates the wave that grows up gradually from an initial stage of the calculation.

At $t = 0.140$ s some small waves are generated near the inlet of the tube and each wave has a coherent shape that the front of the wave inclines ahead a little near the bottom. The liquid film spreads only up to about $\theta = 50°$. At $t = 0.160$ s a relatively large wave (A) begins to spread liquid film in the circumferential direction. At $t = 0.170$ s the liquid film of the wave (A) reaches to about 110°. The maximum value of the film thickness at this moment is 11.2 mm, and the wave height is rapidly growing compared with that at $t = 0.160$ s. On the other hand, the film thickness in the

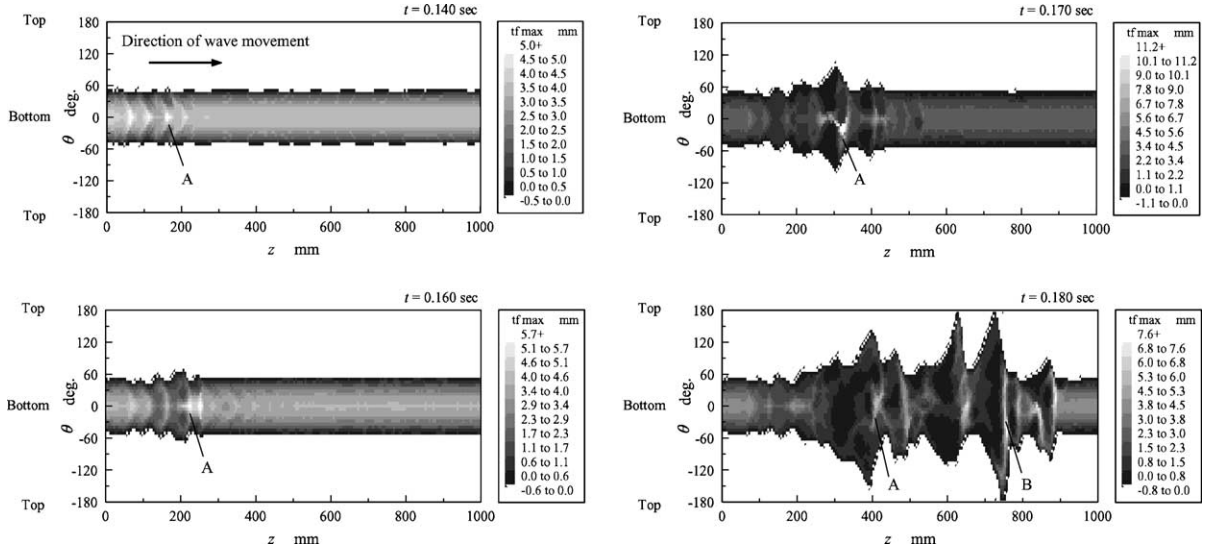

Fig. 6. Change in the film thickness distribution.

upstream side of the wave is thin, within 1.1 mm. Newly growing waves also begin to observe in the downstream region. At $t = 0.180$ s about five large waves appear, two of which reach even the top of the tube.

As clearly seen in Figs. 3 and 5 even the largest wave is not a liquid slug which occupies the whole cross-section of the tube. Then the large waves are considered to be disturbance waves. The shape of each large wave is similar also the scale is different. That is, the film is thick at the crest of the wave and thin in its back even at the bottom. The liquid film spreads rapidly and circumferentially from the bottom of the tube to the top on the front side of the large wave, and narrows gently from the top toward the bottom on the rear side of the wave. This is because the liquid film is left behind the large wave as the wave moves and flows downward as a liquid film by the gravitational force.

4.2. Growing process of single wave

The overall behavior of the growing waves is discussed in the previous section. In this section, we will pay attention to the single wave designated as (B) in Fig. 6 and consider the process of the annular flow formation. Fig. 7 show the growing process of the wave. Within the axial length of 160 mm only the wave (B) is tracked and it moves downstream side by 20 mm in 0.002 s with showing its growing process. The ratio of the unit length of the vertical axis expressed by the sector angle to that of the horizontal axis is unity. To facilitate the comparison between the film thickness distribution shown in Fig. 7 and the pressure distribution shown in Fig. 8, the mark "X" is put at the corresponding point of the maximum height of the wave.

At $t = 0.176$ s a small wave begins to generate near the bottom of the tube. The wave spreads in the circumferential direction at $t = 0.178$ s and the liquid film reaches up to about $\theta = 140°$. It continues to quickly develop and it reaches to the top of the tube at $t = 0.180$ s. The wave with a

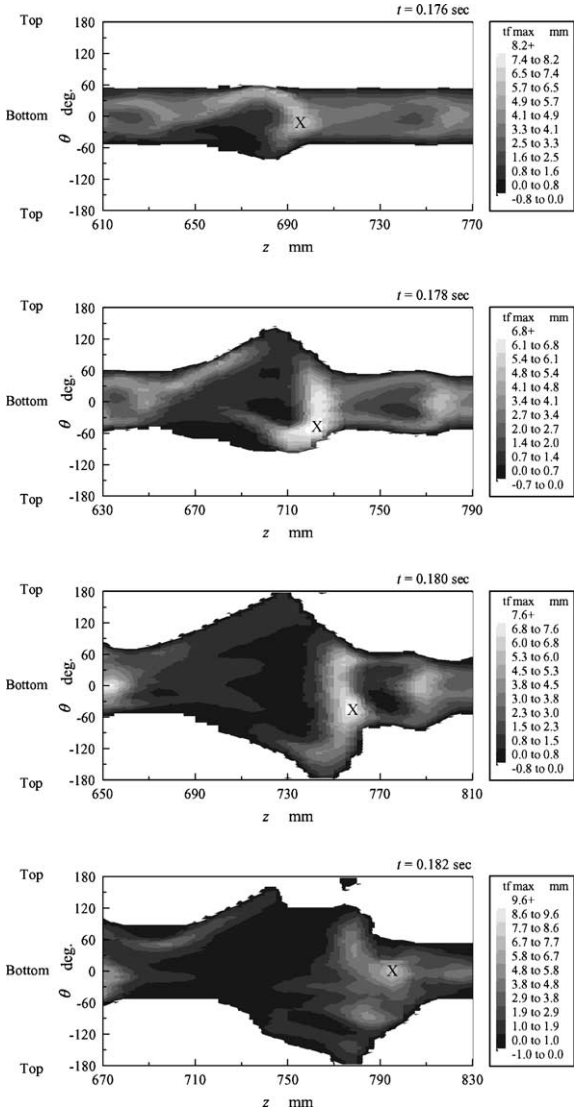

Fig. 7. Film thickness distribution on the interface of developing wave.

large height still exists, but the film thickness is extremely thin in the back of the large wave even at the bottom. In short time the liquid film in the region of $\theta > 0°$ falls downward a little along the tube wall by the gravity force, and it seems to be gradually left behind the large wave at $t = 0.182$ s. Still, however, the liquid film is formed up to $\theta > 150°$, and the structure of an annular flow is kept. On the other hand, the liquid film on the side of $\theta < 0°$ is kept up to the top, and not left behind the large wave. And accordingly the overall shape is seen to be a coherent inclined ring with flowing ahead a little near the bottom. Moreover, the large wave gradually approaches a small wave which begins to develop in $z \fallingdotseq 740$ mm at $t = 0.176$ s, and absorbs it at $t = 0.182$ s. Therefore, the height of the large wave becomes larger at $t = 0.184$ s.

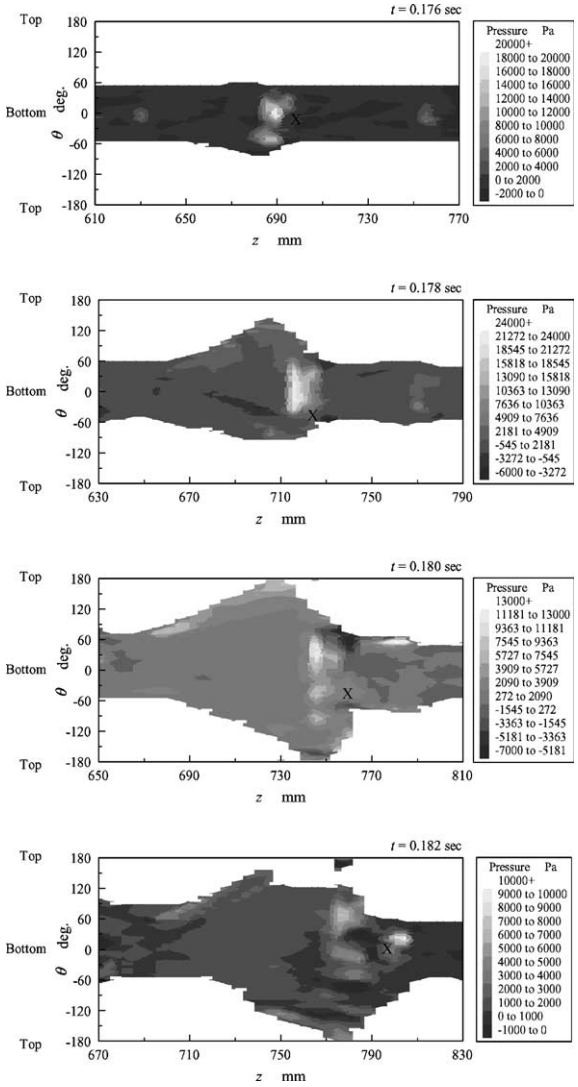

Fig. 8. Pressure distribution on the interface of developing wave.

Next, we will examine the time evolution of the pressure distribution on the interface, and consider what is the main factor for the transport of liquid to the top. Fig. 8 shows the static pressure distribution on the gas–liquid interface by the color map of 12 levels as shown in the right side of each figure. The effect of the pressure loss is excluded here as the same way as Fig. 5.

At $t = 0.176$ s, the high pressure is caused behind the maximum wave height designated by the Xmark, and the pressure gradient between the surroundings is extremely large. And accordingly, the liquid film spreads rapidly in the circumferential direction at $t = 0.178$ s. Here, the liquid film of $\theta > 0°$ reaches the higher position because the pressure gradient is larger in the region of $\theta > 0°$ than that of $\theta < 0°$ at $t = 0.176$ s. The high pressure region behind the wave is caused at the bottom of the tube because the wave height is the maximum and accordingly the stagnation

pressure of the gas flow is the maximum there. On the other hand, the pressure distribution is almost uniform and the film thickness is very small at the back of the large wave. This can be confirmed in each figure.

The static pressure is large just behind the large waves and the pressure gradient is caused in the circumferential direction. That is, this calculation result indicates the same tendency as "the pumping action of the disturbance wave model" which Fukano and Ousaka (1989) proposed. On the other hand, the wave exactly inclines ahead near the bottom of the tube as seen in Fig. 7. And it may seems that liquid is transferred toward the top by the circumferential component of the force acting on the inclined wave by the gas flow. It is the wave spreading mechanism which Butterworth and Pulling (1972) have proposed.

Experimental results shows that the large wave is actually inclined with the front being ahead near the bottom of the tube, and the large waves travel with the circumferentially coherent structure keeping constant. That is, any part of the large wave, from the bottom to the top, moves with the same speed. The present calculation also shows the same tendency as the model of Jayanti et al. (1990). This structure of the large wave is formed as the result that the liquid is transferred continuously from the bottom of the tube to the top. It is not correct that the speed of the disturbance wave is faster at the bottom than at the top, then the disturbance wave is inclined. If the wave spreading model of the large wave is correct, the large wave must lost its coherent structure and disappear in a short time. In the following sections we will examine the mechanism of the liquid flow more in detail.

4.3. Pressure distribution in r–z cross-section

Fig. 9(a) and (b) show simultaneously the film thickness and the static pressure distributions in the r–z cross-section of five different sector angles, which correspond to the case at $t = 0.180$ s in Figs. 7 and 8. The pressure increment for same color level in Fig. 9(a) is smaller in order to show in detail the pressure distribution in the gas phase, while it is larger in Fig. 9(b) to investigate mainly the pressure in the liquid film of the large wave.

The sharp pressure gradient, like pressure jump, in the gas flow is caused across the crest of the large wave as clearly seen in Fig. 9(a). The boundary between the high and the low pressure is at almost the same cross-section, signifying that it is not influenced by the inclination of the wave. The uniform pressure distribution in any r–z plane is caused in the downstream region from this boundary except in the liquid film. On the other hand, the pressure is high and not uniform behind the large wave for $\theta = 0$–$90°$ because the stagnation region in the gas flow is generated there. The pressure distribution is similar because the wave height is almost the same for $\theta = 0$–$45°$. In Fig. 9(b), the pressure is high in the liquid film for $\theta = 0$–$45°$ because the stagnation region is generated behind the large wave and the wave height is large. Therefore, the pressure gradient within the large wave is caused in the circumferential direction between 45° and 90°.

4.4. Velocity distribution in r–θ cross-section

Fig. 10 shows the film thickness and the velocity distributions, viewing from the inlet, in each cross-section of the tube in the front and the rear of the large wave (B) at $t = 0.180$ s in Figs. 6–9, i.e., $z = 670$ and 780, as well as $z = 730$ mm where liquid film form on the whole circumferential of

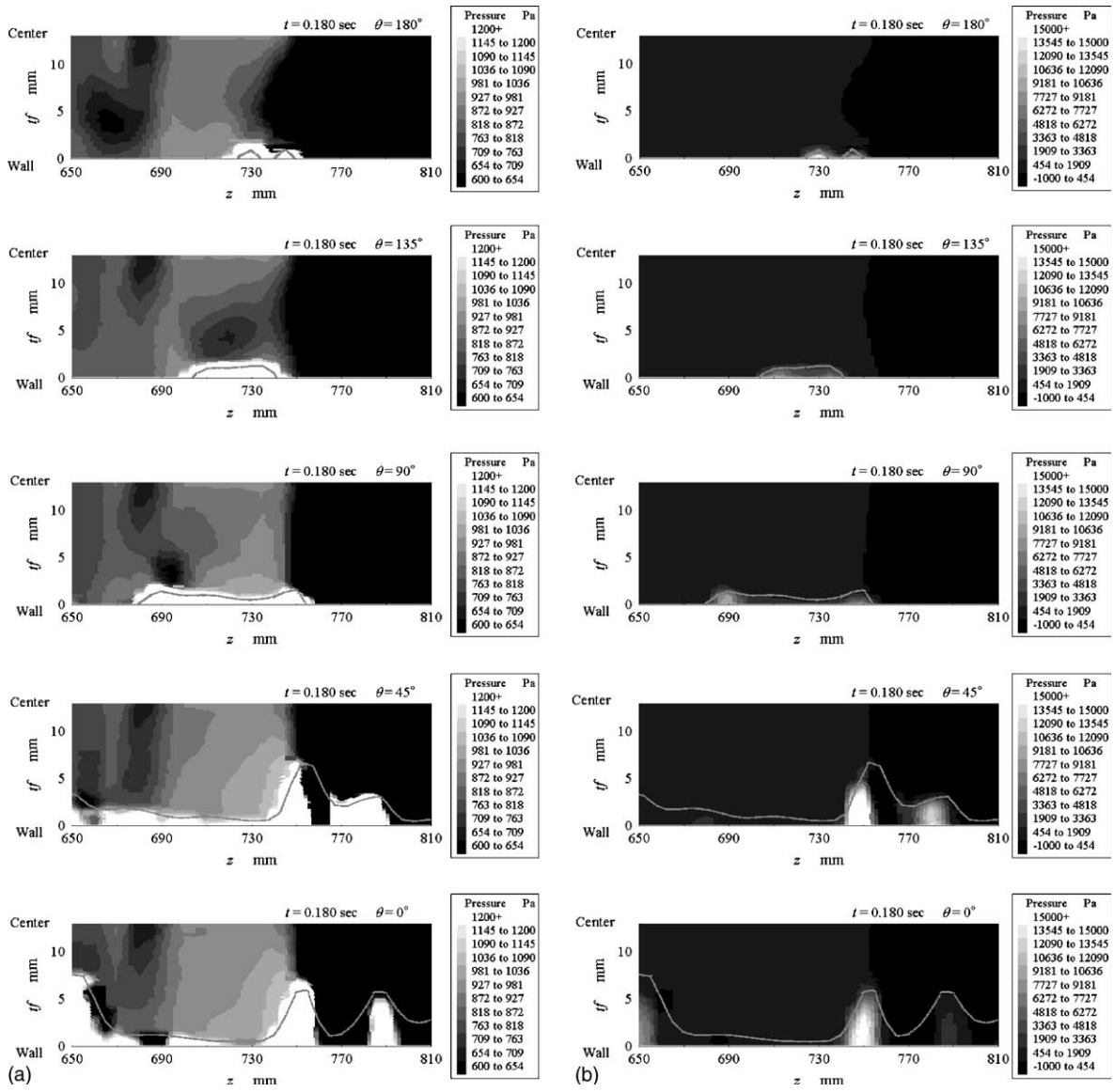

Fig. 9. Pressure distribution. (a) High-lighted in the gas phase in r–z cross-section at $t = 0.180$ s. (b) Pressure distribution high-lighted in the wave in r–z cross-section at $t = 0.180$ s.

the tube. In the cross-section at $z = 670$ and 780 mm, the downward flow of gas is caused near the tube wall, especially near the edge of the liquid film, by which the liquid film seems to be depressed downward. On the other hand the upward gas flow is caused near the interface in the cross-section at $z = 730$ mm, by which the shear force acting on the liquid film seems to play the role to keep the liquid film formation toward the top of the tube. The velocity within the liquid film, however, is larger near the wall than near the interface. And accordingly, it is difficult to conclude that the interfacial shear force due to the secondary gas flow is the predominant factor. As shown in the

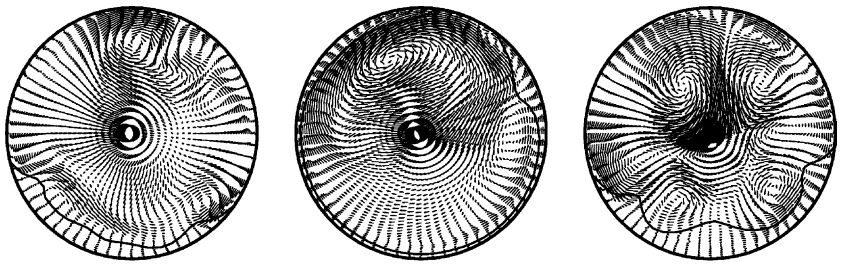

Fig. 10. Velocity distribution in r–θ cross-section at $t = 0.180$ s.

previous section, the larger velocity near the wall is controlled by the pressure gradient in the circumferential direction formed in the large wave. In the cross-section at $z = 780$ mm, which is located just in front of the wave, it is clearly seen that a large couple of vortex exists in the gas phase, and the downward velocity is caused near the wall.

In the secondary gas flow mechanism it is considered that liquid is transferred toward the top of the tube by large shear force acting continuously on the interface due to the steady secondary gas flow. And Lin et al. (1985) assumed that liquid near the wall flows downward by the the gravity force. In the present calculation, however, the upward gas velocity is occasionally caused only near the large wave and the downward velocity at the front and the behind the large wave. In addition, liquid near the wall does not always flow downward but oppositely moves toward the top with larger velocity near the tube wall than near the interface. This means that the secondary gas flow is not the main factor for the liquid film formation toward the top of the tube. Here, the upward velocity of the gas phase near the interface in the cross-section at $z = 730$ mm is caused by the pressure gradient just behind the large wave as shown in Fig. 9(a). This upward flow is a part of the pumping action mechanism which Fukano and Ousaka (1989) proposed.

4.5. Velocity and pressure distribution in θ–z cross-section

From the investigation of the velocity and the pressure distributions in the r–z cross-section discussed above, it was clear that the pressure gradient in the circumferential upward direction plays an important role for the liquid film formation. To examine this mechanism further in detail, we will focus the attention on the velocity relative to one large wave and the pressure distribution near the wall in the θ–z cross-section. Fig. 11 shows the liquid velocity relative to the large wave (B) and the pressure distribution in the θ–z cylindrical surface at $r_w = 0.45$ mm from the wall at $t = 0.178$ s in Figs. 7–10. Here, the wave speed is considerably larger than that of the experimental result and it is about five times; i.e. 13.27 m/s. This is due to that the wave is not fully developed because the calculation is an initial stage. The velocity and the pressure distribution are shown only in the area where the liquid film exists, and the white area means that the liquid film does not exist on the cylindrical surface of $r_w = 0.45$ mm.

Fig. 11 shows that liquid in front of the large wave is transferred at first toward the top by the pressure gradient along the inclination of the wave. Then it generally tends downstream direction near the bottom of the tube after passing by the large wave. That is, the liquid flows into and out

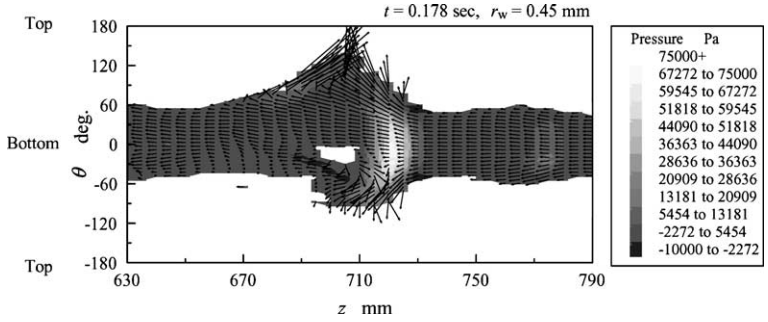

Fig. 11. Distribution of relative velocity and pressure in θ–z cross-section at $t = 0.178$ s.

of the large wave, around which a part liquid spreads in the circumferential direction by the large pressure gradient from the bottom to the top of the tube cross-section. This liquid film gradually falls downward by the gravitational force after reaching the top and being left behind the large wave.

4.6. Mechanism of liquid film formation

The aspect of flow of both phases in case of $j_G = 30$ m/s and $j_L = 0.06$ m/s was investigated in the r–z, the r–θ, and the θ–z cross-sections, respectively, and it was clarified that the pressure gradient plays an important role in the liquid film formation up to the top of the tube. Taking into these information, we will propose the mechanism of the liquid film formation.

Liquid flow observed from a relative frame of reference fixed to the large wave is drawn in Fig. 12(a) and (b), as a side view and a top view, respectively. The base film flows into the front and out of the rear of the large wave. The pressure across the wave crest in the gas flow discontinuously changes because the gas flow separates just in front of the wave, and accordingly the pressure is almost uniform near the front side of the wave. On the other hand, the pressure is high at the stagnation point of the gas flow behind the large wave. The pressure gradient within the traveling large wave is induced along the wave to the top by the stagnation pressure of gas flow. The

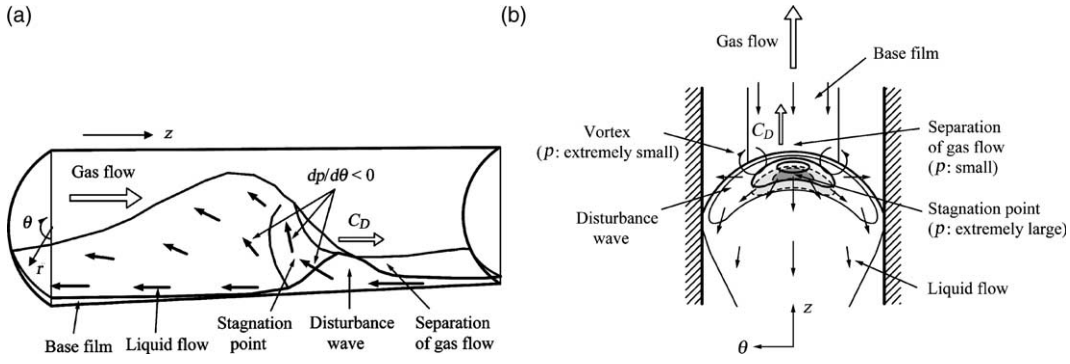

Fig. 12. Present flow model. (a) Bird's-eye view of the relative flow to the large wave traveling to the right. (b) Relative flow viewed from the top of the tube.

pressure is the largest near the bottom and gradually decreases in the circumferential direction as the wave height decreases toward the tube top. By that pressure gradient, liquid is transported from the bottom to the top forming a disturbance wave. Hence, the disturbance wave has a ring type coherent shape which inclines backward and travels with the same velocity at any part of the coherent large wave, i.e., without decay. This flow model obtained by the present DNS is almost similar to the pumping action model which Fukano and Ousaka (1989) have proposed.

5. Conclusions

In the present study, DNS analysis of the horizontal gas–liquid two-phase annular flow was done to clarify the mechanism of the liquid film formation and the following results were obtained.

(1) Annular flow was calculated by using the present numerical technique, and the liquid film formation toward the top of the tube was reproduced.
(2) The numerical analysis is possible even in the case of the high Reynolds number and the large density ratio between gas and liquid.
(3) The large waves have the shape that incline ahead a little and the circumferentially coherent waves travel with the same speed.
(4) Liquid is transferred toward the top by the pressure gradient induced by the gas flow within the large wave in the circumferential direction.
(5) The secondary gas flow is not generated in the entire region of the tube but only near the back of the large wave.
(6) The circumferential velocity in the annular liquid film is larger near the wall than near the interface. This shows that the shear force by the secondary gas flow is not the main factor for the liquid film formation.
(7) The droplet deposition is not the predominant factor for the liquid film formation in the present case of the relatively small tube diameter because the annular liquid film is formed although the droplets cannot be captured by this calculation technique.
(8) The pumping action model which Fukano and Ousaka (1989) have proposed is the most predominant one for the mechanism of the liquid film formation in a horizontal annular flow.

References

Amsden, A.A., Harlow, F.H., 1970. The SMAC method: a numerical technique for calculating incompressible fluid flows. LA-4370.

Butterworth, D., Pulling, D.J., 1972. A visual study of mechanisms in horizontal annular air–water flow. AERE-M2556.

Chang, Y.C., Hou, T.Y., Merriman, B., Osher, S., 1996. A level set formulation of eulerian interface capturing methods for incompressible fluid flows. J. Comput. Phys. 124, 449–464.

Flores, A.G., Growe, K.E., Griffith, P., 1995. Gas-phase secondary flow in horizontal, stratified and annular two-phase flow. Int. J. Multiphase Flow 21, 207–221.

Fukano, T., Ousaka, A., 1989. Prediction of the circumferential distribution of film thickness in horizontal and near-horizontal gas–liquid annular flows. Int. J. Multiphase Flow 15, 403–419.

Fukano, T., Ousaka, A., Morimoto, T., Sekoguchi, K., 1983. Air–water annular flow two-phase flow in a horizontal tube (Part 2. Circumferential variations of film thickness parameters). Bull. Jpn. Soc. Mech. Engrs. 26, 1387–1395.

Jayanti, S., Hewitt, G.F., White, S.P., 1990. Time-dependent behaviour of the liquid film in horizontal annular flow. Int. J. Multiphase Flow 16, 1097–1116.

Kawamura, T., Kuwahara, K., 1984. Computation of high Reynolds number flow around a circular cylinder with surface roughness. AIAA Paper 84-0340.

Laurinat, J.E., Hanratty, T.J., Jepson, W.P., 1985. Film thickness distribution for gas–liquid annular flow in a horizontal pipe. Physicochem. Hydrodyn. 6, 179–195.

Lin, T.F., Jones, O.C., Lahey, R.T., Block, R.C., Murase, M., 1985. Film thickness measurements and modeling in horizontal annular flows. Physicochem. Hydrodyn. 6, 197–206.

Osher, S., Sethian, J.A., 1988. Fronts propagating with curvature-dependent speed: algorithms based on Hamilton–Jacobi formulations. J. Comput. Phys. 79, 12–49.

Ousaka, A., Fukano, T., Morimoto, T., 1985. Air–water two-phase annular flow in a horizontal tube and near horizontal tubes (hold-up, frictional pressure drop and circumferential distribution of film thickness). Trans. Jpn. Soc. Mech. Engrs. 51, 2728–2736 (in Japanese).

Russell, T.W.F., Lamb, D.E., 1965. Flow mechanism of two-phase annular flow. Can. J. Chem. Eng. 43, 237–245.

Sussman, M., Smereka, P., Osher, S., 1994. A level set approach for computing solutions to incompressible two-phase flow. J. Comput. Phys. 114, 146–159.

Sutharshan, B., Kawaji, M., Ousaka, A., 1995. Measurement of circumferential and axial liquid film velocities in horizontal annular flow. Int. J. Multiphase Flow 21, 193–206.

Verzicco, R., Orlandi, P., 1996. A finite-difference scheme for three-dimensional incompressible flows in cylindrical coordinates. J. Comput. Phys. 123, 402–414.